DEEP UV LED DYNAMIC OPTICAL IMAGING AND FLUORESCENCE SPECTROSCOPY OF THE PROTEIN CORONA IN A PLASMONIC SOLUTION AND THE EFFECT OF NEAR-INFRARED LASER HEATING

M. E. Khosroshahi [1,2*], V. Woll-Morison [1]

[1] Nanobiophotonics & Biomedical Research Laboratory, M.I.S. Electronics Inc., Richmond Hill, Ontario, Canada; e-mail: khosrom@mie.utoronto.ca, m.khosro@miselectronics.com
[2] Department of Mechanical and Industrial Engineering, University of Toronto, Ontario, Canada

When plasmonic nanoparticles (PNPs) enter a biofluid, the adsorbed biomolecules on the surface form a protein corona, which has direct consequences in biomedical applications. The binding in passive adsorption is nonspecific and is governed by ionic, van der Waals, and hydrophobic forces. We describe the results of deep LED (275-nm) interaction with bovine serum albumin (BSA) containing gold nanourchin (GNU) using dynamic beam view profiling and fluorescence spectroscopy. 800-nm diode laser-induced thermal effects on the bioplasmonic solution were investigated using probe beam monitoring and an IR camera. The results indicated a consistent nonlinear and oscillatory behavior of the GNU-BSA complex due to the adsorption and desorption process of protein. Tyrosine (Tyr) fluorescence enhancement and quenching were observed, which can provide some information about the binding kinetics and protein conformational changes. After 10 min of laser heating, the Tyr fluorescence completely vanished and the He-Ne probe beam was broadened by about 4 nm owing to molecular collisions and protein denaturation. The temperature variation due to protein unfolding and denaturation exhibited a similar nonlinear pattern at different GNU volumes. However, the temperature was lower at higher GNU concentrations, indicating a higher rate of protein adsorption, which effectively mitigated the localized surface plasmon resonance heating.

Keywords: *protein corona, gold nanourchin, bovine serum albumin, fluorescence spectroscopy, optical imaging, thermal effects.*

ГЛУБИННАЯ УФ-СВЕТОДИОДНАЯ ДИНАМИЧЕСКАЯ ОПТИЧЕСКАЯ ВИЗУАЛИЗАЦИЯ И ФЛУОРЕСЦЕНТНАЯ СПЕКТРОСКОПИЯ КОРОНЫ БЕЛКА В ПЛАЗМОННОМ РАСТВОРЕ И ЭФФЕКТ НАГРЕВА ИЗЛУЧЕНИЕМ ЛАЗЕРА В БЛИЖНЕЙ ИК-ОБЛАСТИ

M. E. Khosroshahi [1,2*], V. Woll-Morison [1]

УДК 535.372:547.96

[1] M.I.S. Electronics Inc., Онтарио, Канада;
e-mail: khosrom@mie.utoronto.ca, m.khosro@miselectronics.com
[2] Университет Торонто, Онтарио, Канада

(Поступила 9 февраля 2021)

Исследовано взаимодействие светодиодного глубинного УФ-излучения (275 нм) с бычьим сывороточным альбумином (БСА), содержащим наночастицы золота (НЧЗ), с использованием динамического профилирования луча и флуоресцентной спектроскопии. Тепловое воздействие излучения диодного лазера с λ = 800 нм на биоплазмонный раствор исследовано с помощью мониторинга зондирующего луча и ИК-камеры. Результаты показали последовательное нелинейное и колебательное поведение комплекса НЧЗ-БСА из-за процесса адсорбции и десорбции белка. Наблюдаемые усиление и тушение флуоресценции тирозина (Tyr) могут дать информацию о кинетике связывания и конформационных изменениях белка. После лазерного нагрева в течение 10 мин флуоресценция Tyr полностью исчезает и зондирующий пучок He–Ne расширяется на ~4 нм из-за столкновений молекул и денатурации белка. Изменение температуры вследствие разворачивания и денатурации белка демонстрирует аналогичную нелинейную картину при разных объемах НЧЗ. Однако температура ниже

при более высоких концентрациях НЧЗ, что указывает на более высокую скорость адсорбции белка, способствующую уменьшению локализованного поверхностного плазмонного резонанса посредством нагревания.

Ключевые слова: *корона белка, наночастица золота, бычий сывороточный альбумин, флуоресцентная спектроскопия, оптическая визуализация, тепловой эффект.*

Introduction. During the last decade, nanotechnology has played a significant role in technological advancement and various applications in nanomedicine and biomedical engineering, including biology [1], diagnosis [2], imaging [3–5], photothermal therapy [6, 7], and pharmaceutical and drug delivery [8–10]. In a number of papers, features of nanostructures (NS; their optical properties and surface chemistry, limitations, and advantages) are investigated. It was found that certain critical criteria exist that ought to be considered before their use, namely, biocompatibility, noncytotoxicity, biodegradability, immunogenicity, surface properties, drug loading capacities and release, drug stability, and storage of NS [11, 12]. Among the variety of NS, plasmonic nanoparticles such as gold nanoparticles (GNPs) meet the above requirements and exhibit unique physical properties compared with bulk counterparts, owing to their large surface area and high surface free energy. The main advantages of their optical properties include surface-enhanced scattering, nonlinear optical properties, tunable resonance in visible near-infrared (Vis-NIR) spectroscopy, and time-dependent properties because of the adjustable nanoparticle size and shape [13–15]. It is known that during the interaction of the electromagnetic wave with GNPs, the conduction band electrons are excited, causing a coherent oscillation that exhibits strong optical absorption and scattering because of localized surface plasmon resonance (LSPR) [16]. Owing to plasmon oscillation, an induced dipole enhances the local electric field at the surface of the GNPs. Thus, strong light absorption and scattering occur at the SPR frequency, which is temperature dependent [15, 17]. However, in the case of the biomedical applications of NS, as soon as they enter a biological environment such as our body, their identity significantly changes owing to the formation of a biomolecular layer such as protein known as corona. Figure 1 is a schematic representation of corona formation on gold nanourchin (GNU).

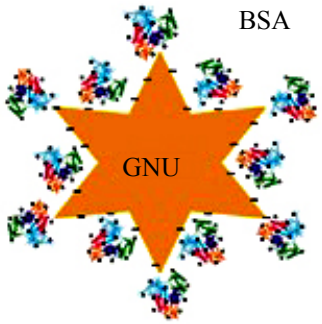

Fig. 1. Schematic representation of protein corona around gold nanourchin.

This affects the size, charge, or aggregation of the nanocarriers, hence the fate of payload, which in turn determines the efficacy of drug delivery, cellular uptake, toxicity, and in vivo distribution. It is suggested that if proteins are smaller than the NS, they may be stretched to cover the surface, and if they are larger, then the NS may decrease the mutual interaction causing fewer structural changes [18]. Moreover, the protein adsorption is strongly dependent on the shape of the nanoparticles [19]. The corona is characterized by the density, thickness, composition, and relative abundance of each protein. In this research, bovine serum albumin (BSA) is used as the protein, which is the most abundant plasma protein. It consists of a single chain of 583 amino acid residues. It is a negatively charged, nonglycosylated globular protein with a single polypeptide chain containing three α-helical domains with a diameter of ~10 nm. Another interesting type of nanostructure is GNU, with a spiky uneven surface, which causes a redshift in the surface plasmon peak. This nanostructure possesses a larger surface, an enhancement of the electromagnetic field at the sharp tips, and thus higher heat generation compared with spherical GNPs [20]. Spectroscopic techniques such as absorption and fluorescence can monitor the changes in optical signals and the surface density of BSA on GNP and in addition study multiple adsorbate molecules. The goals of this research are to (a) investigate the time-resolved corona conformational changes on GNU in PBS using a wavefront sensor, UV-Vis, and fluores-

cence spectroscopy; (b) study dynamic laser-induced heating effects on the fluorescence emission and the GNU-BSA complex using an 800-nm diode laser at various powers.

Materials. 20 mL of citrated GNUs with a 100-nm diameter dispersed in 0.1 mM phosphate-buffered saline were purchased from Cytodiagnostics (GU-100-20; Burlington, ON, Canada). The corresponding particle and weight concentrations are 3.84×10^{9} NP/mL, and 3.89×10^{-2} mg/mL, respectively. Phosphate buffer saline (PBS, pH 7.4, Gibco) and bovine serum albumin (BSA, A2153-10G, Sigma-Aldrich) with an isoelectric point between 4.5 and 4.9 were used as the matrix solution and the protein source. For UV-Vis spectroscopy, a concentration of 4 g/L (i.e., 1.5 mL PBS and 6 mg BSA) was prepared, and for fluorescence spectroscopy three concentrations were prepared: two samples with a concentration of 4 g/L (with and without 0.1 mL of GNU), and the third sample with a concentration of 4.7 g/L with 0.1 mL of GNU.

Experimental. The absorbance of PBS+BSA and PBS+BSA+GNU was measured by a UV-Vis spectrometer (Jenway 205-Cole-Parmer, Montreal, QC, Canada) within the 198–1000 nm spectral range. A quartz cuvette 1 cm in width (Cole-Parmer, Montreal, QC, Canada) containing the medium was irradiated by a deep UV 275-nm LED (CUD7GF1BCT-ND; Digi-Key, Thief River Fall, MN, USA). A CMOS-based Shack-Hartmann wavefront sensor (WFS; 150-50C; Thorlabs, Newton, NJ, USA) with 300–1100 nm spectral sensitivity was used to investigate the corona changes as a function of intensity distribution in the optical beam. The WFS was placed behind the cuvette directly facing the LED so that the micro-lens array of the sensor produces a matrix of focal spots on the camera. The unwanted back reflections into the source were reduced by slightly tilting the WFS. The off-center beam was measured after the full beam had been contained within the active sensor area. This was checked by verifying that the power density distribution was displayed in the beam view panel. The image acquisition was controlled by the WFS software, which also analyzed the centroid locations of the focal spots. The beam views were then saved and analyzed by the computer. The induced fluorescence was guided by a 400-μm optical fiber to the UV-Vis spectrometer (FLAME-T-XR1-ES, Ocean Optics) equipped with a 2048-pixel linear silicon CCD array (14×200 μm) with a detector range of 200–1050 nm and an optical resolution of 1.5 nm full width half maximum (FWHM). The output of the spectrometer was analyzed by a laptop computer. A four-channel fiber-coupled laser (MCLs1; Thorlabs, Newton, NJ, USA) with a stable, low-noise, and 20 mW output operated at 808 nm as the pump beam. For delivery of this beam, a silica fused optical cable with a 0.39 numerical aperture (Thorlabs, Newton, NJ, USA) and a 400-μm core diameter was used. This beam was applied to study the thermal effects on the fluorescence of PBS+BSA, studying the probe beam (a 632-nm He-Ne, 5-mW laser [R-36602; Newport, Irvine, CA, USA]), passing through the sample containing 0.1 mL GNU (the output was detected by a UV-Vis spectrometer [Flame-T-XRI-ES; Ocean Optics, Orlando, FL, USA]), and measuring the temperature changes in the solution with 0.1 and 0.3 mL of GNU. The temperature was measured by a thermal camera (Fluke-PTi-120).

Results and discussion. The behavior of BSA in an aqueous medium is dependent on various interactions, including electrostatic, hydrogen bonding hydrophobic, and van der Waals. The response of free thiol to the outer surface of globular BSA with the GNU surface can weaken or change the secondary or tertiary structure of the BSA molecules, which can lead to their unfolding from the globular structure [21]. The BSA-GNU conjugates are obtained by passive adsorption where they have stabilized through electrostatic interaction between negatively charged GNU and the positively charged positions of amino acids in the protein such as lysine and histidine (i.e., dipole–dipole attraction) and the hydrophobic interaction between protein and the gold surface. It is thought that once the proteins are adsorbed on the surface of NS, it is possible to undergo a conformational change to a more energetically favorable position to enhance its interaction with the surface. Figure 2a shows an absorption peak of BSA in PBS at 275 nm, which corresponds to Tyr. Figure 2b is the magnified section indicating the two broad bands between 520 and 600 nm with a maximum around 580 nm and the other between 700 and 800 nm respectively. In the former case, the small peak at about 525 nm can correspond to sodium chloride in PBS or other amino acids such as arginine and histidine around 520 nm, which overlap considerably. Moreover, within this range, valine and cystine have close absorbance at 550 nm, and isoleucine has an absorptive peak at 580 nm. The second band originates from the PBS composition, possibly corresponding to disodium phosphate. Figure 2c represents the absorbance for combined BSA and 0.1/0.3 mL GNU. As is seen, the absorptive intensity is reduced compared with BSA only because of the adsorption at the surface of GNU. Hence, the transmission increases because of less free available BSA in the solution. By the same argument, the intensity is decreased at a higher GNU concentration. It is noteworthy that at 0.1 mL, the two peaks observed in Fig. 2d are identical to those in Fig. 2b. However, at 0.3 mL a peak at about 680 nm also appears. It corresponds to the SPR of GNU.

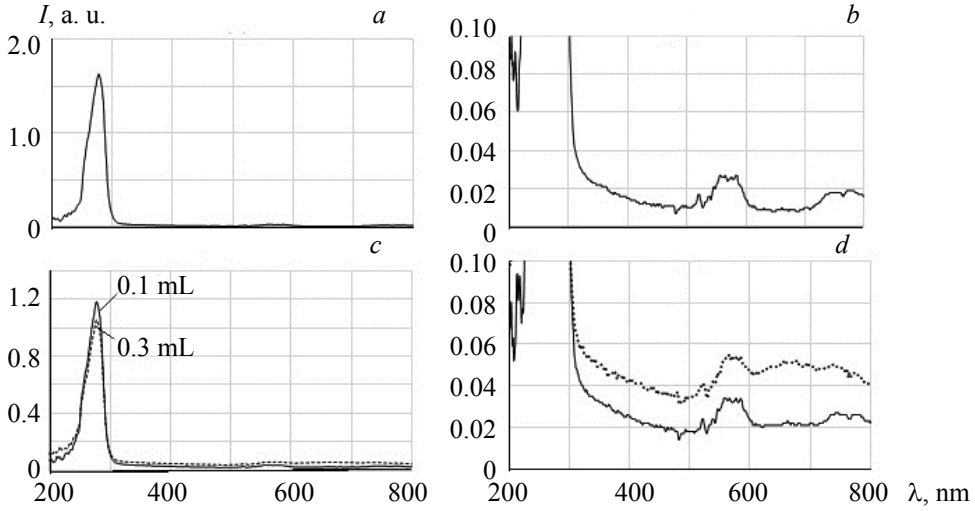

Fig. 2. (a) UV-Vis absorbance of BSA in PBS with a sharp peak at 275 nm corresponding to Tyr, (b) magnified of (a) with two peaks between 520–600 and 700–800 nm, (c) the absorbance of combined BSA and GNU using 0.1 and 0.3 mL, and (d) magnified of (c) with an extra peak corresponding to GNU.

The spatial intensity distribution of a 275-nm LED probe beam due to changes of the corona is represented in Fig. 3. Here, the sample is irradiated during the 600 s. The beam view panel provides an overview of the intensity distribution within the active camera sensor area. Different colors in the spectrum represent the intensity distribution in the beam caused by the interaction region observed by the WFS. For example, green shows the medium distortion, and the red and white represent the highest distorted parts. The probe beam intensity (the size of the red central beam) exhibits an oscillatory nonlinear behavior of the corona that corresponds to adsorption (decreasing) and desorption (increasing). Indeed, desorption due to dipole-dipole repulsive forces indicates the conformational changes and the change in positions (orientation of dipoles within the protein molecules). Therefore, the corona is not a fixed layer but is constantly changing and its composition is determined by the kinetics rate of desorption and the desorption of proteins.

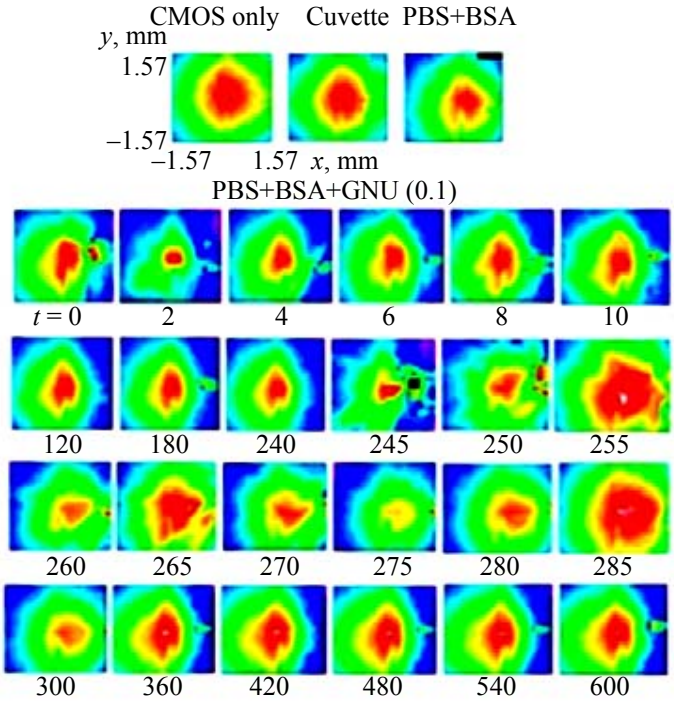

Fig. 3. The beam profile of the sensor showing the time-resolved spatial intensity distribution of LED inside the solution demonstrating the oscillatory behavior of BSA.

The changes in the corresponding peak-to-valley (PV) amplitude represented in Fig. 4a are caused by wave front distortion because of aberration fluctuation owing to the changes in the corona thickness. There are three distinct zones denoted I, II, and III representing the corresponding changes between 0 and 250, 250, and 300, and 300 and 600 s, respectively. Figure 4b shows the enlarged version of zone I with a sharp decrease, i.e., a deep valley between 4 and 8 s. The enlarged form of this section is seen in Fig. 4c as zone II. It is interesting to note the sharp rise between 255 and 260 s in Fig. 4d, beyond which it remains almost constant for 15 s, followed by a dip for 5 s, and then it rises again.

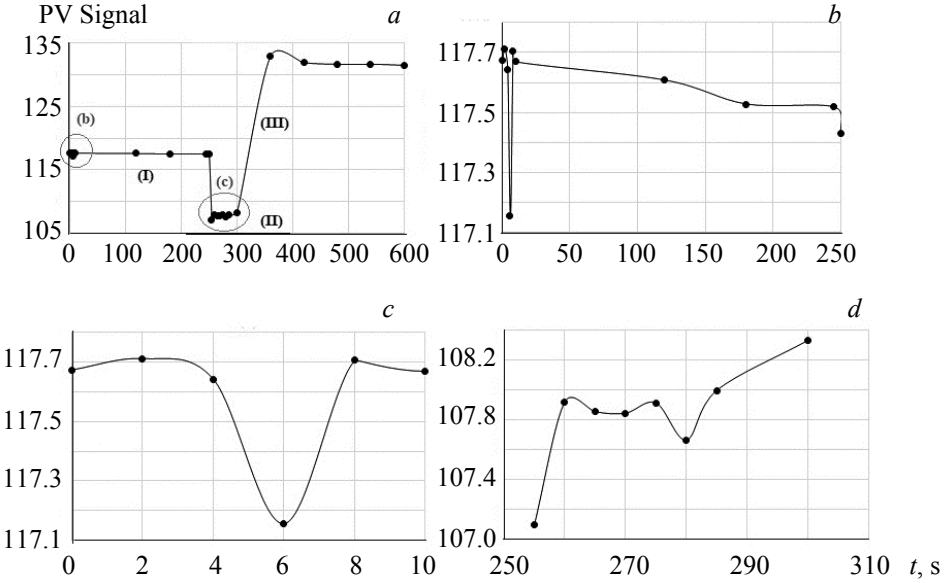

Fig. 4. Variation of the corresponding peak-to-valley amplitudes of the beam profiles in Fig. 4, (b) the enlarged version of zone I with a sharp decrease i.e., a deep valley between 4–8 s, (c) the enlarged form of (b) seen as zone II, and (d) a sharp rise between 255–260 s beyond which it relatively remains constant for 15 s and followed by a dip for 5 s then it rises again.

The fluorescence of a folded protein is due to a mixture of individual aromatic residues. The intrinsic fluorophores of BSA mainly include tyrosine (Tyr), tryptophan (Trp), phenylalanine (Phe), and disulfide bonds that can be excited to an upper electronic state, during which they undergo a conformational change. Within nanoseconds, they return to the ground state via vibrational relaxation emitting a characteristic wavelength, which can be used as a diagnostic of the conformational state of a protein. Figure 5a, calculated for 4 g/L of BSA without GNU and the excitation wavelength at 275 nm, demonstrates two emission peaks (one of them at 300 nm corresponds to Tyr and another weaker one at 380 nm likely indicates the presence of Trp or L-alanine acid). Figure 5b is the time-resolved spectra for the sample with 0.1 mL of GNU studied for 13 min. Here, the initial peak gradually increases from blue (1) to green (2), and red (3). The increase in fluorescence emission represents the protein unfolding, particularly Tyr, which can be exploited for probing structural rearrangements of proteins in addition to the extensively used Trp emission. However, when the experiment was repeated with 4.7 g/L (i.e., an extra 1 mg of BSA), in Fig. 5c, we observed that the main peak corresponding to Tyr at about 300 nm quenched step-wise from purple (1) to light blue (5) with a relatively larger decrease from (4) to (5). At this stage, the peak increased from (5) to red (6) and then decreased again to yellow (7). Clearly, such an oscillatory response demonstrates the folding and unfolding of the molecular structure due to quenching and enhancement. Other varying influencing factors include quantum yield, corona thickness due to adsorption and desorption, turbidity, and optical path length. The fluorescence of amino acids is strongly dependent on the polarity of its local environment. In fact, the fluorescence of a folded protein is a mixture of the fluorescence from individual aromatic residues. Most of the intrinsic fluorescence emissions of a folded protein are due to the excitation of Tyr, Trp, and, to a lesser extent, Phe.

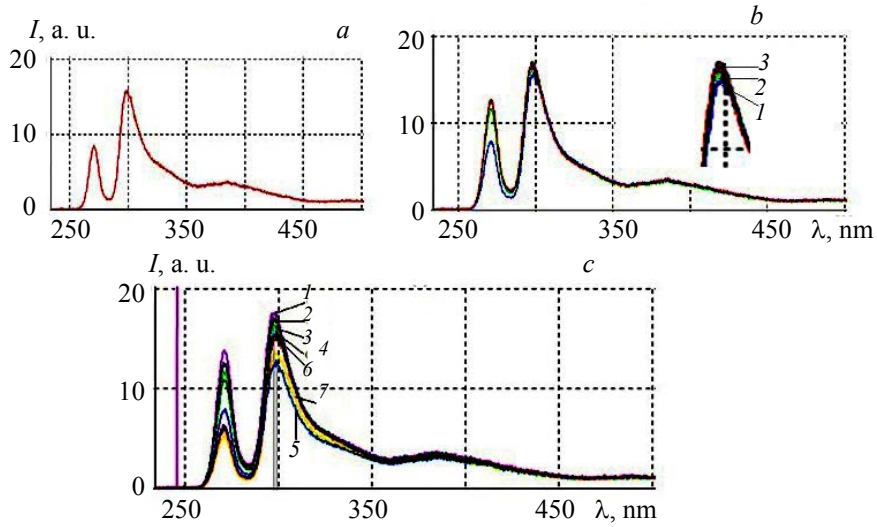

Fig. 5. (a) The fluorescence of BSA without GNU with the excitation wavelength at 275 nm and two emission peaks at 300 and 380 nm likely corresponding to Try or L-Alani acid, respectively, (b) the time-resolved spectra for the sample using 4 g/L with 0.1 mL of GNU studied for 13 min with enlarged section seen as inset. Note the increasing trend of peaks, (c) using 4.7 g/L, the intensity of peaks first decreased from (1) to (5), then increased from (5) to (6) and finally decreased from (6) to (7).

It is noteworthy that plasmon-enhanced fluorescence, which originates from the local field enhancement of the incident light, can also play a role in fluorescence enhancement. Upon interaction of light with plasmonic nanoparticles, local surface plasmon oscillations are formed, which are collective oscillations of conduction band electrons that produce an intense electromagnetic local field in the vicinity of nanoparticles with exponential spatial variation, known as near-field $\bar{E}_n$ [22]:

$$\bar{E}_n = \frac{\left|\bar{E}_l(x,\lambda_{\text{ex}})e_p\right|^2}{\left|\bar{E}_o\right|^2}, \tag{1}$$

where $\bar{E}_o$ and $\bar{E}_l$ are the amplitudes of the incident and local enhanced fields in the position of the molecule, x is the nanoparticle-emitter distance, and e_p is the emitter's orientation. The coupling of $\bar{E}_n$ enhances the incident field and consequently improves the absorption and the quantum yield of the fluorophore. Thus, the enhanced emission of the excited molecule is proportional to $(\langle|E^2\rangle P_0)Q\varepsilon cl$, where Q is the number of photons emitted/number of photons absorbed is the quantum yield, ε is the molar absorption coefficient ($M^{-1} \cdot cm^{-1}$), c is the molar concentration of the analyte (g/L), l is the optical path length, and P_0 is the initial excitation power. Despite the dynamic state between GNU and the molecules, if the molecules become very close (<10 nm) or directly attached to the surface of GNU, then quenching occurs [23]. This is thought to represent the changes that occur in the structure of BSA, such as unfolding, during the interaction with GNU [24–26]. In addition, the decrease in fluorescence intensity (Fig. 5c) is related to the hydrodynamic diameter of GNU. Therefore, measurements of fluorescence quenching can provide some information about the protein-particle binding kinetics, protein conformational changes, and absorbance, as well as the relative accessibility of GNU to protein chromophore groups [27, 28].

The NIR laser-induced heating effect on the fluorescence is shown in Fig. 6, where shows the initial state of PBS+BSA with peaks at 300 and 380 nm, and then a gradual decrease until they completely disappear after 3 min of exposure. It is suggested that dynamic temperature quenching is accompanied by an energy transfer from Tyr to Trp, which is related to the mobility changes of groups within the protein molecule structure [29, 30] and to thermal unfolding transitions of proteins [29].

Figure 7a shows no probe beam broadening in the PBS+BSA solution for 1 h of irradiation. But when 0.1 mL of GNU was added, the width began to change and was broadened by 2 nm at FWHM after 10 min (Fig. 7b). The beam was further broadened by 4 nm after 40 min of heating, as shown in Fig. 7c. Two major factors can explain this effect: thermal collision, and protein unfolding, i.e., geometrical shape factor.

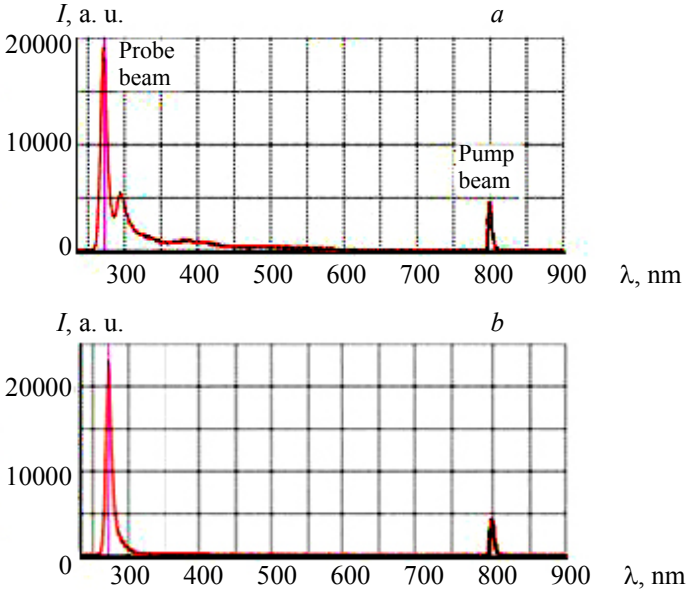

Fig. 6. NIR laser-induced heating effect on the fluorescence (a) shows the initial state of PBS+BSA with peaks at 300 and 380 nm, and (b) the peaks disappear after three minutes of laser exposure.

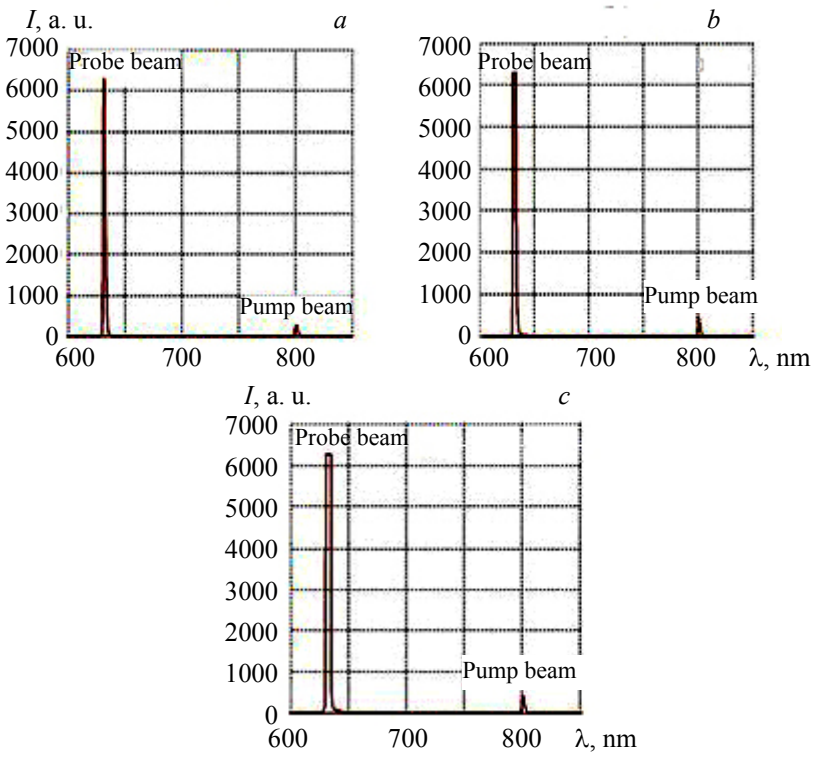

Fig. 7. (a) No probe beam broadening in PBS+BSA solution during an hour of irradiation, (b) the width of beam was broadened by 2 nm when 0.1 mL of GNU was added and heated for 10 min and (c) 40 min.

It is known that the atoms and molecules of the liquids and gases are in continuous motion and collide frequently, and it is further enhanced by thermal excitation governed by the Maxwell–Boltzmann distribution. Heat can disrupt hydrogen bonds and nonpolar hydrophobic interactions. This occurs because heat increases the kinetic energy and causes the molecules to vibrate so rapidly and violently that the bonds are disrupted.

Therefore, some deformation of the particles can perturb the energies of the outer electrons and hence the line width:

$$\Delta\upsilon_m = \frac{2\pi k_B T(\Delta\upsilon_c)}{P_0}, \tag{2}$$

where $\Delta\upsilon_m$ is the line width at FWHM, k_B is the Boltzmann constant, T is the temperature, P_0 is the laser power, and $\Delta\upsilon_c = 1/2\pi\tau_c$, where τ_c is photon decay time. In addition, the effect of unfolding of the protein structure can enhance the beam broadening via optical scattering, as BSA is an orientation-dependent structure and, therefore, the scattering intensity distribution depends on the angle of incidence. In this case, if we assume that $\sum_c(\mathbf{X})$ represents the cross-sectional area of BSA molecules per unit volume, which in fact indicates the geometric attenuation coefficient in the beam direction , then this parameter can be resolved into two different components given as an integral over all possible orientations of the BSAs in the PBS volume [31]:

$$\sum_c(\mathbf{X}) = \int_u n(\mathbf{u})\sigma_c(\mathbf{u}, \mathbf{X})d\mathbf{u}. \tag{3}$$

Here, $n(\mathbf{u})$ indicates the number of BSAs per unit volume with orientation $\mathbf{u}$, and $\sigma_c(\mathbf{u},\mathbf{X})$ corresponds to the cross-sectional area of BSA when exposed to light in the ($\mathbf{X}$) direction. The value of $\sigma_c(\mathbf{u},\mathbf{X})$ mainly depends on the geometrical shape of the molecules interacting with light, i.e., the shape or structure factor $S(\mathbf{q})$ quantifies the effect of the spatial random organization of the scatterers on the backscattering coefficient β' [32]:

$$\beta' = n(\mathbf{u})S(\mathbf{q})\sigma\beta', \tag{4}$$

where $\sigma_{\beta'}$ is the backscattering cross-section of a single scatterer. As the hydrodynamic diameter of GNUs becomes larger, the condition $2\pi R_p/\lambda > 1$ is fulfilled, where R_p is the radius of GNU. Thus, the intensity distribution of light increases in the forward direction and the cosine of scattering phase function for small angles is much larger than for all other angles. Figure 8a indicates the variation of the temperature of the solution with exposure time at different concentrations of GNU. It is interesting to note that:

1. The temperature variation within the experimental error exhibits a nonlinear and stochastic response, which, in turn, demonstrates the random nature of the results due to the non-uniform distribution of GNU.

2. The oscillatory behavior of adsorption and desorption of proteins can directly affect the results, as in the case of fluorescence spectroscopy.

3. Data represent the density and distribution of GNUs at that particular instant of time and position during the interaction. For longer time periods, the temperature of a spatially localized volume element may be different owing to some agglomeration and possible thermal overlapping of a larger fraction of GNUs and clustering at that element [5, 33].

4. There is a pattern similarity between the results at both concentrations, particularly the peaks and valleys, which may correspond to desorption (i.e., higher plasmonic temperature) and adsorption (i.e., lower plasmonic temperature) respectively.

5. The temperature at a lower concentration is higher, which indicates that a higher volume fractional heat is generated.

The thermal images of the samples heated by a laser for 20 s show the lowest temperature rise of ~24°C for PBS+BSA only (Fig. 8b). When 0.1 mL of GNU was added, the temperature increased to ~26°C (Fig. 8c), but using 0.3 mL of GNU caused the temperature to decrease again to ~25°C (Fig. 8d).

For a single GNU exposed to a laser beam the generated power is $P = I_0\sigma_\alpha$, where I_0 and σ_α are the initial power density and absorption cross-section respectively given by [34, 35]:

$$\sigma_\alpha = \frac{8\pi^2}{\lambda} R_g^3 \left[\frac{\varepsilon_g(\omega) - \varepsilon_m}{\varepsilon_g(\omega) + 2\varepsilon_m} \right], \tag{5}$$

where ε_g, $\varepsilon_m = \varepsilon_g/2$ are permittivity of GNU and the surrounding medium respectively, and R_g is the GNU radius. The heat, produced per unit volume, is $Q_g = P/V_g$, where V_g is the volume of the GNU, and the heat source, derived from the heat power density, is $Q_\rho = \int_v Q_\rho(r)d^3r$, where the integral is over the GNU volume.

If all the absorbed optical energy is converted to nanoparticle heating, the temperature increase can be evaluated using [35]:

$$\Delta T_{\max} = P\sigma_\alpha / c_g m_g, \tag{6}$$

where m_g is the mass, and c_g is the specific heat capacity of GNU. Assuming that there are no phase transformations at a given power, heat transfer in a system with GNU thermal sources is described by the heat conduction equation:

$$\rho_g(r)c_g(r)\frac{\partial T(r,t)}{\partial T} = K_m\nabla^2 T(r,t) + Q_s(r,t)\,, \tag{7}$$

where $T(r,t)$ is the temperature, $\rho_g(r)$ is the density and specific heat of GNU respectively, K_m is the thermal conductivity of the surrounding medium, and $Q_s(r,t)$ is the heat source. The physical significance of $K_m\nabla^2 T(r,t)$ is observed as 3-D heating of the surrounding (Fig. 8c), where heat is conducted well beyond the cylindrical beam geometry. The optical interaction and the photothermal effects under the plasmon resonance conditions are strongly dependent on the size and shape of the nanoparticle. Also, the clusters can result in enhanced thermal effects as heat flow from individual NPs can be added [36]:

$$Q(r,t) = \sum_n q_n(t)\delta(r - r_n)\,, \tag{8}$$

where $q_n(t)$ represents the heat produced by n-GNU, r is the coordinate position, i.e., the distance from the center of GNU, and the heat generated by the ensemble per unit time is [34]:

$$Q(r,t) = -\frac{1}{2}\mathrm{Re}\left[i\omega\frac{\varepsilon_P(\omega)-1}{4\pi}\right]\sum_n\int \tilde{E}(r)\tilde{E}^*(r)d^3r\,. \tag{9}$$

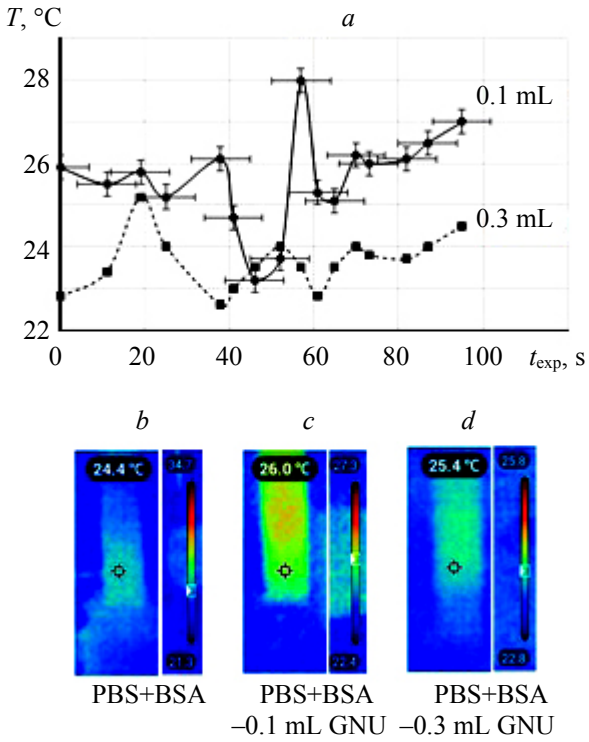

Fig. 8. (a) Variation of solution temperature with exposure time at different concentrations of GNU. The thermal images of samples heated by laser for 20 s (b) temperature rises to ~24°C for PBS+BSA, (c) to ~26°C when 0.1 mL of GNU was added, (d) with 0.3 mL of GNU, the temperature decreased again to ~25°C.

Finally, the interaction of PNPs with a biomolecular environment (such as protein) can be studied theoretically by modeling the protein coverage θ and hydrodynamic diameter ϕ_h of GNU [37]:

$$\phi_h = \phi_0\sqrt[3]{[1+\gamma\ \theta]}\,, \tag{10}$$

where ϕ_0 is the GNU diameter,$\gamma = V_P/V_{NP}$ is the scaling constant (volume ratio of protein molecules to GNU) [38], $V_P = M_w/\rho_p N_A \approx 8.3\times10^{-29}$ m^3 is the volume of protein, the molecular weight M_w of BSA ≈66.5 g/mol, $\rho_P = 1320$ kg/m^3 is the density of the protein, $N_A = 6.022\times10^{23}$ mol^{-1} is Avogadro's number, and

$V_{NP} = (4/3)\pi R_{NP}^3 \approx 5.2\times10^{-22}$ m^3 is the volume of GNU. Thus, $\gamma \approx 1.6\times10^{-7}$. The protein coverage θ (the maximum number of adsorbed molecules per GNU) is described by the Hill equation [39, 40]:

$$\theta = \frac{(P_c)^n}{(P_c)^n + (K_d)^n}, \tag{11}$$

where P_c is the free protein concentration. So, the molarity $M \approx 0.06$ and 0.071 mol/L for 4 and 4.7 g/L respectively, n is the Hill coefficient representing the number of binding sites/particles, $K_d = 1/K_b$ is the dissociation constant, and K_b is the binding constant. Assuming the values of $n \approx 0.8$ and $K_d \approx 10^{-6}$ M for BSA adsorption on citrated-stabilized GNU [40], then by substituting the values in Eq. (11) and modeling using MATLAB-R202a-9.8, it is shown that θ increases asymptotically and soon approaches unity at higher concentration values (Fig. 9a). This is equivalent to about 3.5-nm protein coverage at the above protein concentrations using Eq. (10), as shown in Fig. 9b.

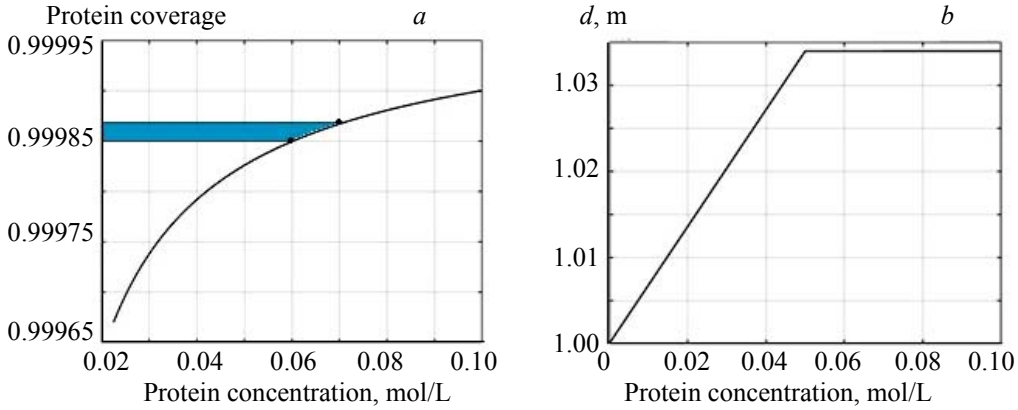

Fig. 9. Modeling (a) the hydrodynamic diameter d of GNU+BSA complex and (b) the protein coverage at the surface of GNU using MATLAB software.

Conclusions. We demonstrate that beam view imaging and fluorescence spectroscopy can provide useful information regarding the protein interaction with the gold nanourchin ensemble, and bovine serum albumin conformational changes. Oscillatory behavior of the corona and nonlinear fluorescence variation was observed. The thermal heating caused the fluorescence quenching and the nonlinear (in type) temperature changes at different concentrations of gold nanourchin. However, at a higher concentration the temperature decreased, probably because of a thicker layer of the corona shielding effect. Modeling showed a hydrodynamic change of about 3 nm and that about 85% of the gold nanourchin surface was covered under our conditions.

Acknowledgements. The authors would like to thank and acknowledge MIS Electronics Inc. for funding the research at the Nanobiophotonics & Biomedical Research Lab.

REFERENCES

1. J. Albanese, P. Tang, W. Chan, *Ann. Rev. Biomed. Eng*., **14**, 1–16 (2012).
2. K. Jain, *Clin. Chem*., **53**, 2002–2009 (2007).
3. P. Sharma, S. Brown, G. Walter, S. Santra, *Adv. Colloid Interface Sci.*, **471-485**, 123–126 (2016).
4. Y. Huang, Sh. He, W. Cao, K. Cai, X. Liang, *Nanoscale*, **4**, 6135 (2012).
5. M. E. Khosroshahi, A. Mandelis, B. Lashkari, *J. Biomed. Opt.*, **20**, 076009 (2015).
6. V. Pattani, J. Tunnell, *Lasers Surg. Med.*, **44**, 675–684 (2012).
7. M. E. Khosroshahi, Z. Hassannejad, M. Firouzi, A. Arshi, *Lasers Med. Sci.*, **30**, 1913–1922 (2015).
8. J. Estelrich, E. Escribano, J. Queralt, *Int. J. Mol. Sci*., **16**, 8070–8101 (2015).
9. M. E. Khosroshahi, L. Ghazanfari, Z. Hassannejad, S. Lenhert, *Nanomed. Nanotech*., **6**, 1–9 (2015).
10. J. Finbloom, F. Sousa, M. Stevens, T. Desa, *Adv. Drug Deliv. Rev.*, **167**, 89–108 (2020).

11. P. Tartaj, M. Morales, S. Verdaguer, T. Gonzaleze-Carreno, C. Serna, *J. Phys. D: Appl. Phys*., **36**, R182–183 (2003).
12. R., Gref, Y. Minamitake, M. Peracchia, V. Trubetskoy, V. Torchilin, *Science*, **263**, 1600–1603 (1994).
13. P. Jain, P. Seok, I. El-Sayed, M. El-Sayed, *J. Phys. Chem. B*, **110**, 7238–7248 (2006).
14. C. Noguez, *J. Phys. Chem.*, **111**, 3806–3819 (2007).
15. Z. Hasannejad, M. E. Khosroshahi, *Opt. Mat.*, **35**, 644–651 (2013).
16. K. Willets, R. Van Dune, *Ann. Phys. Rev. Chem*., **58**, 267–297 (2007).
17. V. Pustovalov, V. Babenkov, *Laser Phys. Lett.*, **10**, 516–520 (2004).
18. P. Koegler, A. Clayton, H. Thissen, *Adv. Drug Del.*, **64**, 1820–1839 (2012).
19. M. Zehfus, G. Rose, *Biochemistry*, **25**, 5759–5765 (1986).
20. R. Rodriguez-Oliveros, J. Sanchez-Gill, *Opt. Exp.*, **20**, 621–626 (2012).
21. D. Tsai, F. DelRio, A. Kneene, K. Tyner, *Langmuir*, **27**, 2464–2477 (2011).
22. D. Darvill, A. Centeno, F. Xie, *Phys. Chem. Chem. Phys.*, **15**, 15709–15726 (2013).
23. Sh. Pawar, A. Bhattacharya, A. Nag, *ACS Omega*, **4**, 5983–5990 (2019).
24. N. Zhdanova, E. Shirshin, E. Maksimov, I. Panchishin, V. Fadeev, *Photochem. Photobiolog. Sci.*, **1**, 1–32 (2013).
25. M. Losin, F. Toderas, S. Astilean, *J. Mol. Struct.*, **924-926**, 196–200 (2009).
26. G. Mandal, M. Bardhan, T. Ganguly, *Colloids Surf. B: Biointer.*, **81**, 178–184 (2010).
27. D. Gao, Y. Tian, S. Bi, Chen, Y. *Spectrochem. Acta A*, **62**, 1203–1208 (2005).
28. D. Jang, M. Elsayed, *Proc. Nat. Acad. Sci. USA*, **86**, 5815–5819 (1989).
29. M. Eftink, *Biochem.*, **30**, 8945–8953 (1991).
30. A. B. Ghisaidoobe, S. Chung. *Int. J. Mol. Sci.*, **15**, 22518–22538 (2014).
31. B. Khlebtsov, N. Khlebtsov, *J. Quant. Spectr.*, **106**, 154–169 (2007).
32. M. Fribel, A. Roggen, G. Muller, *J. Biomed. Opt.*, **11**, 034021 (2006).
33. M. E. Khosroshahi, *Appl. Phys. B*, **125**, 229 (2019).
34. G. Baffou, R. Quidant, *Laser Photon. Rev.*, **7**, 171–187 (2013).
35. V. Pustovalov, V. Babenko, *Laser Phys. Lett.*, **2**, 84–89 (2005).
36. A. Govorov, W. Zhang, T. Skeini, H. Richardson, J. Lee, A. Kotov, *Nanoscale Res. Lett*., **1**, 84–90 (2006).
37. M. Lacerda, A. Karim, J. Douglas, D. Pristinski, *ACS Nano*, **4**, 365–379 (2010).
38. H. Moustaoui, J. Saber, I. Djeddi, Q. Liu, D. Movia, *Nanoscale*, **11**, 3665–3673 (2019).
39. C. Röcker, M. Pötzl, W. Parak, U. Nienhaus, *Nature Nanotech. Lett.*, **4**, 577–580 (2009).
40. M. Cui, R. Liu, Zh. Deng, G. Ge, *Nano Res.*, **7**, 345–352 (2014).